The essential role of carefully optimized synthesis for elucidating intrinsic material properties of (Ga,Mn)As

P. Němec,[1] V. Novák,[2] N. Tesařová,[1] E. Rozkotová,[1] H. Reichlová[2,1], D. Butkovičová[1], F. Trojánek,[1] K. Olejník,[2] P. Malý,[1] R. P. Campion,[3] B. L. Gallagher,[3] Jairo Sinova,[4,2] and T. Jungwirth[2,3]

[1] *Faculty of Mathematics and Physics, Charles University in Prague, Ke Karlovu 3, 121 16 Prague 2, Czech Republic*

[2] *Institute of Physics ASCR, v.v.i., Cukrovarnická 10, 16253 Praha 6, Czech Republic*

[3] *School of Physics and Astronomy, University of Nottingham, Nottingham NG72RD, United Kingdom*

[4] *Department of Physics, Texas A&M University, College Station, TX 77843-4242, USA*

Supplementary Information

Supplementary Figures

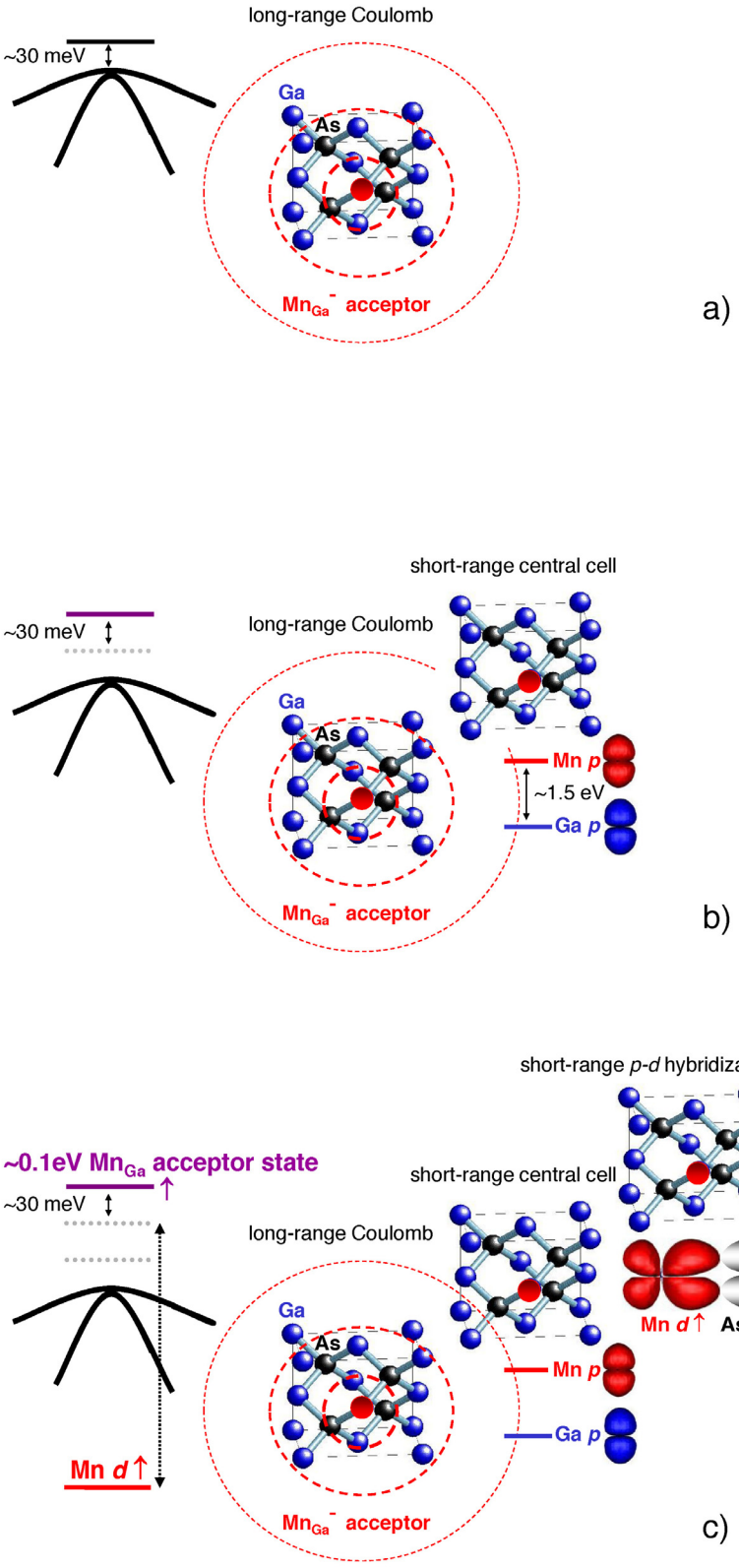

Supplementary Figure S1. Schematic diagrams of the long-range (a) and the two short-range (b), (c) contributions to the single Mn acceptor level. No bound state in the gap would form without the long-range Coulomb potential.[6]

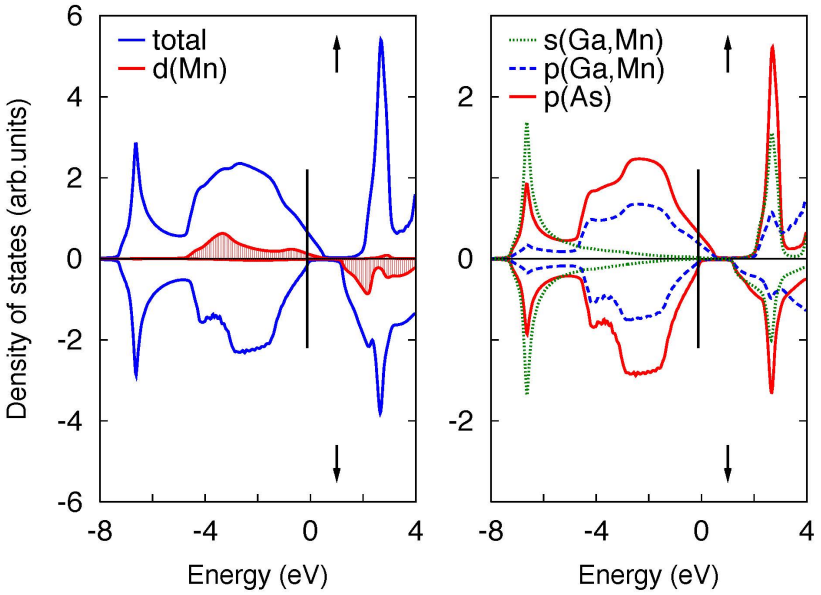

Supplementary Figure S2. Tight-binding approximation density of states of $Ga_{0.9}Mn_{0.1}As$ and its orbital composition. Position of Fermi energy is indicated by a vertical line.[6]

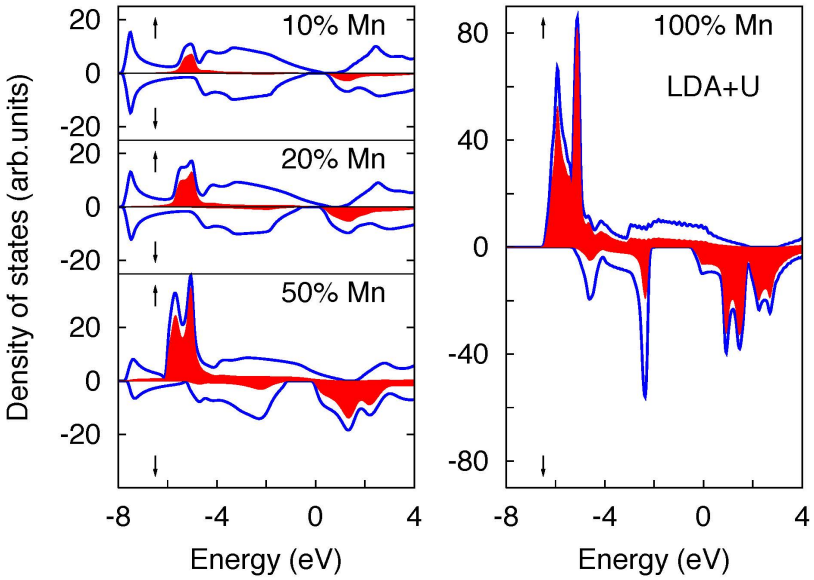

Supplementary Figure S3. Density of states for (Ga,Mn)As mixed crystals with various content of Mn obtained in the LDA+U approximation. Shaded area shows the partial density of Mn d-states.[6]

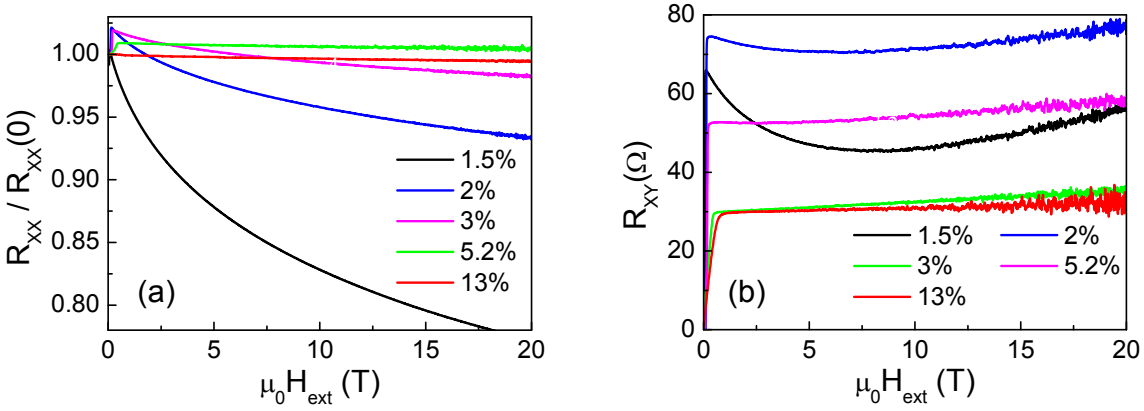

Supplementary Figure S4. Hall effect measurements. (a) Longitudinal resistances R_{xx} [normalized to $R_{xx}(0)$], and (b) transversal (Hall) resistances R_{xy} as a function of normal magnetic field $\mu_0 H_{ext}$ measured in (Ga,Mn)As epilayer with depicted Mn concentration x; samples temperature 4.2 K.

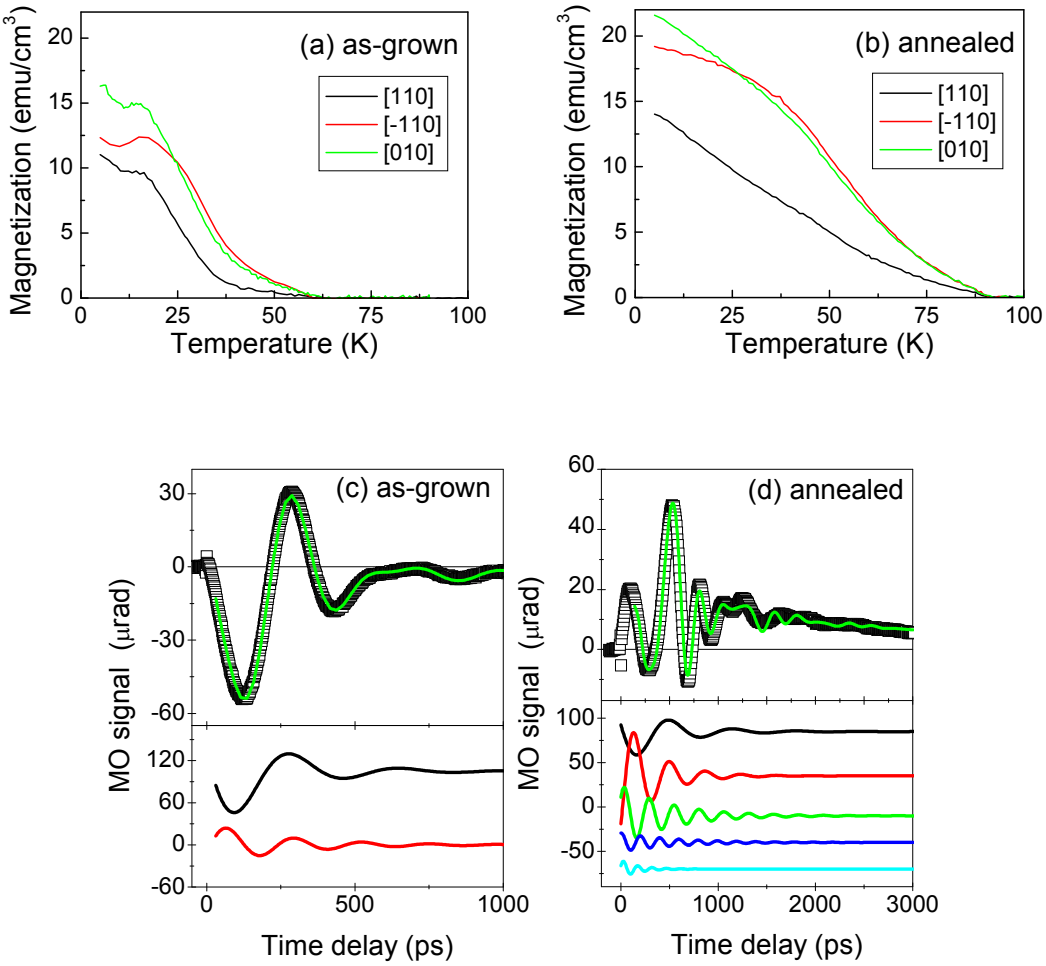

Supplementary Figure S5. Influence of annealing on properties of 500 nm thick (Ga,Mn)As epilayer.
(a) and (b): Temperature dependence of the magnetization projections to different crystallographic directions measured by SQUID in as-grown (a) and annealed for 40 hours at 200°C (b) sample with $x = 7\%$.
(c) and (d): Time-resolved magneto-optical (MO) signals (points) measured in the as-grown (a) and the annealed (b) samples; note the different x-scales in (c) and (d). The lines in the upper parts of figures (c) and (d) are a sum of damped harmonic functions and the corresponding precession modes are plotted in the lower parts of the figures. External magnetic field of 10 mT was applied along the [010] crystallographic direction.

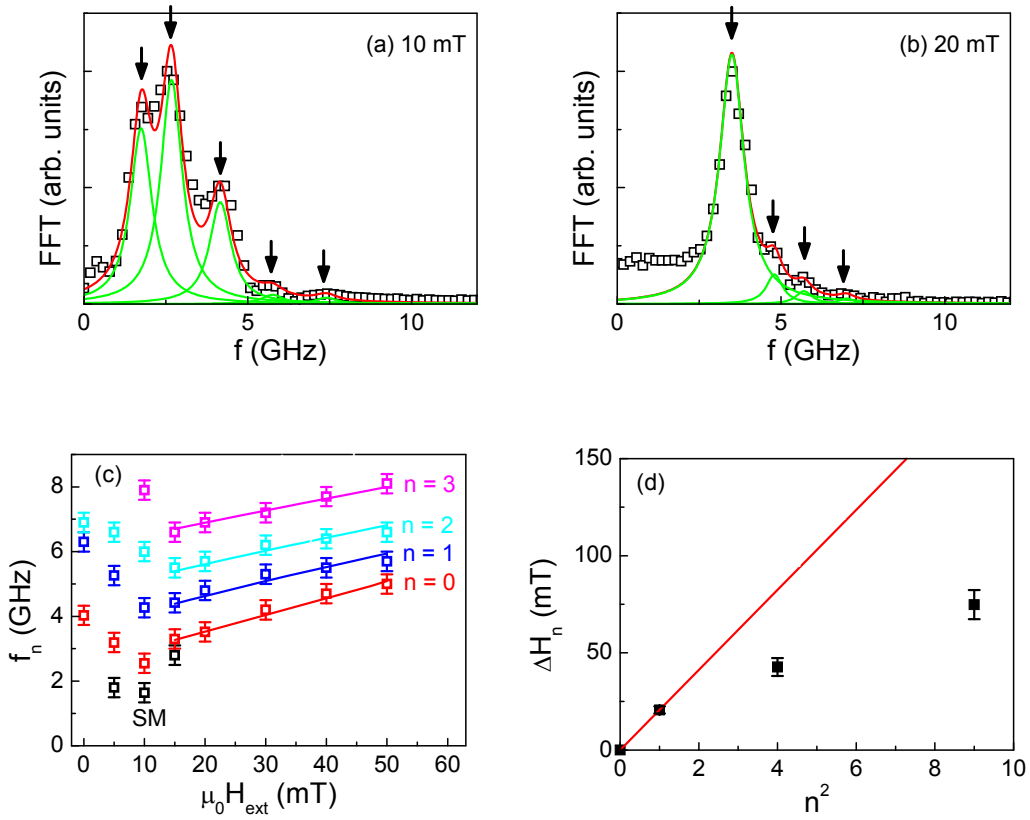

Supplementary Figure S6. Demonstration of inapplicability of spin stiffness measurement in thick (Ga,Mn)As epilayers.
(a) and (b): Fourier spectrum of the oscillatory part of the magneto-optical signal measured in the annealed 500 nm thick sample with x = 7% for external magnetic fields H_{ext} of 10 mT (a) and 20 mT (b) applied along the [010] crystallographic direction (points); the red line is a fit by a sum of Lorentzian peaks (green lines) and the arrows indicate positions of the peak frequencies.
(c) Dependence of the precession frequency f_n on magnitude of external magnetic field applied along the [010] crystallographic direction with a plausible assignment of the measured frequencies to four spin wave resonances (which are labeled by the mode numbers n) and one non-propagating surface mode, SM, (points). Lines are fits by Supplementary Equation S19.
(d) Dependence of mode spacing ΔH_n on square of the mode number n (points), line is the theoretical dependence $\Delta H_n \sim n^2$ that corresponds to D = 60 meV.nm^2.

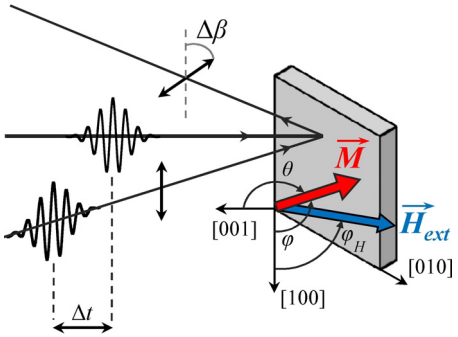

Supplementary Figure S7. Schematic diagram of the magneto-optical experimental set-up. An impact of the femtosecond laser pump pulse induces the magnetization precession in (Ga,Mn)As, which is detected by measuring a rotation of the polarization plane of reflected linearly polarized probe pulses as a function of the time delay Δt between pump and probe pulses. The orientation of magnetization in the sample is described by the polar angle φ and azimuthal angle θ. The external magnetic field H_{ext} is applied in the sample plane at an angle φ_H.

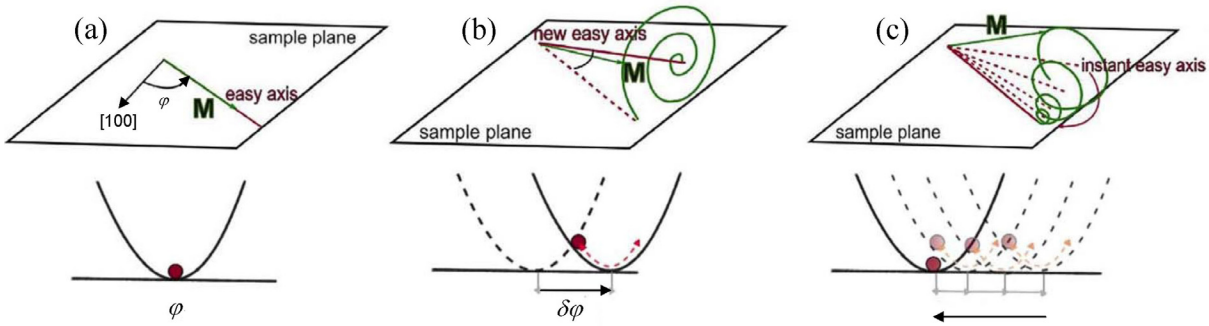

Supplementary Figure S8. **Schematic illustration of the thermal laser pulse-induced precession of magnetization**. (a) In the equilibrium, the magnetization points to the easy axis direction, which is located in the sample plane at azimuthal angle φ. (b) Absorption of the laser pulse leads to a photo-injection of electron-hole pairs. The subsequent fast nonradiative recombination of photo-injected electrons induces a transient increase of the lattice temperature (within tens of picoseconds after the impact of the pump pulse). The laser-induced change of the lattice temperature then leads to a change of the easy axis position. As a result, magnetization starts to follow the easy axis shift by the precessional motion. (c) Dissipation of the heat leads to the return of the easy axis to the equilibrium position. Simultaneously with this, the precession of magnetization is stopped by the Gilbert damping.

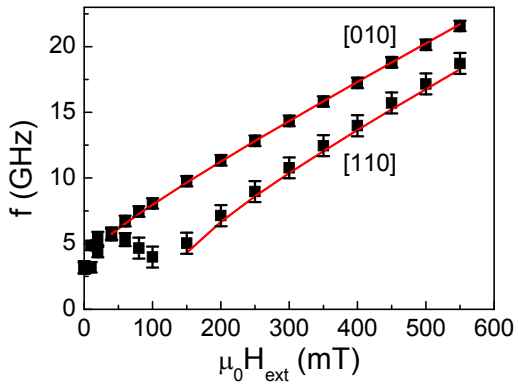

Supplementary Figure S9. **Evaluation of anisotropy fields from precession frequencies**. Dependence of the precession frequency f on external magnetic field H_{ext} applied along the [010] and [110] crystallographic directions in (Ga,Mn)As epilayer with x = 5.2% (points); the lines are fits by Supplementary Equations S14 and S13, respectively, with K_c = 31 mT, K_u = 27.5 mT, and K_{out} = -190 mT.

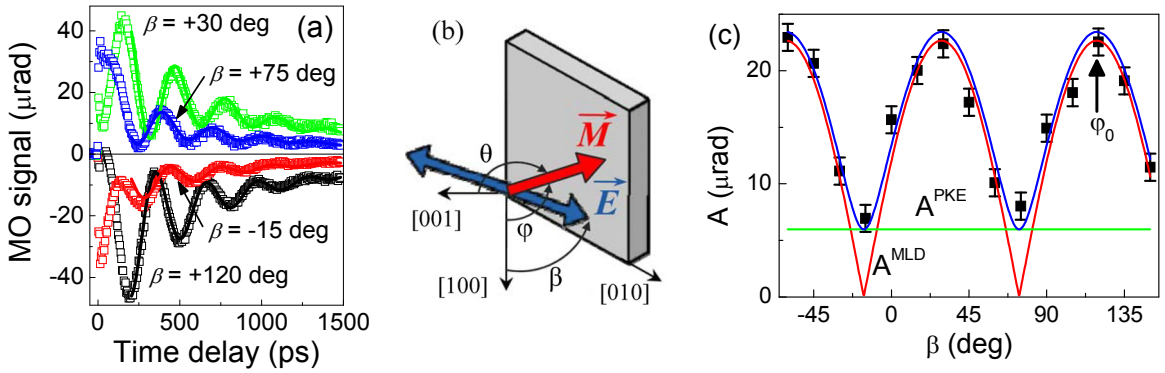

Supplementary Figure S10. **Evaluation of the easy axis position from measured magneto-optical (MO) signals.** (a) Dynamics of the MO signals measured by probe pulses with different probe polarization orientations β in (Ga,Mn)As epilayer with x = 5.2% for $\mu_0 H_{ext}$ = 0 mT (points); lines are fits by Supplementary Equation S16 with parameters f = 3.2 GHz, τ_G = 360 ps and τ_p = 1050 ps. (b) Definition of the angle β that describes the orientation of the probe polarization plane $\boldsymbol{E}$. (c) Probe-polarization dependence of the oscillatory part A of the MO signal that was obtained by fitting the dynamics shown in part (a) by Supplementary Equation S16; the values of A at time delay of 200 ps are shown (points). Lines are fits of $A(\beta)$ by a sum of a polarization-independent signal due to polar Kerr effect (PKE) and a polarization-dependent signal due to magnetic linear dichroism (MLD) (Eq. (2) in Ref. 41). The vertical arrow depicts the deduced easy axis position in the sample without the pump pulse, φ_0.

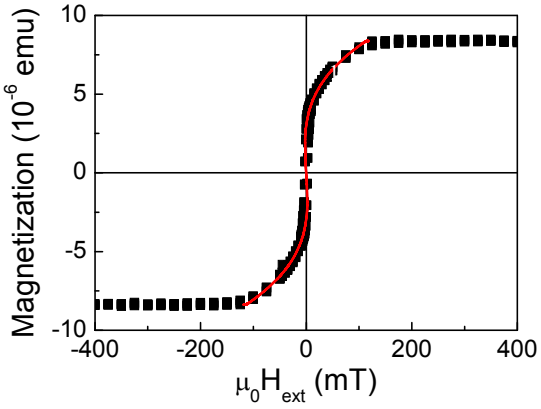

Supplementary Figure S11. **Evaluation of the magnetic anisotropy from SQUID magnetometry**. The SQUID measurement along [110] crystallographic direction in (Ga,Mn)As epilayer with x = 5.2% (points) is compared with the calculated magnetization projection for K_c = 31 mT and K_u = 27.5 mT (line).

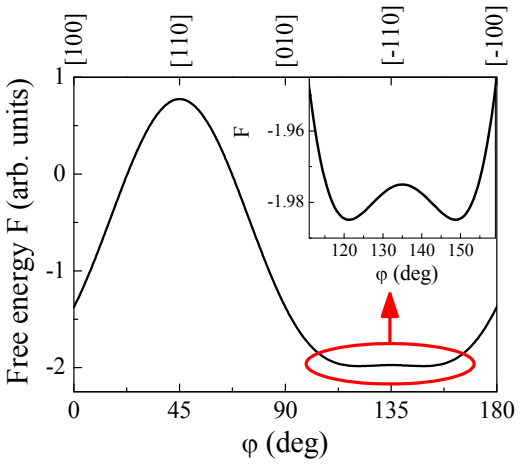

Supplementary Figure S12. Example of the obtained in-plane magnetic anisotropy. In-plane angular dependence of the free energy (Supplementary Equation S5) in (Ga,Mn)As epilayer with x = 5.2%; anisotropy fields K_c = 31 mT and K_u = 27.5 mT.

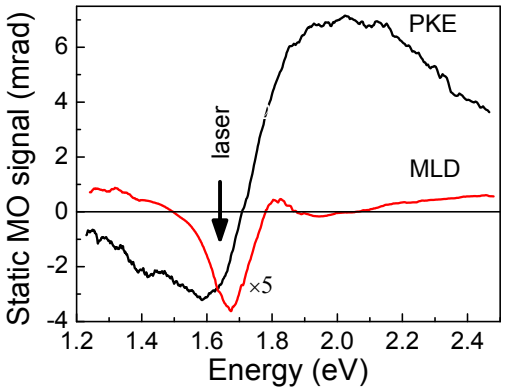

Supplementary Figure S13. **Example of static magneto-optical (MO) spectra.** Spectral dependence of polar Kerr effect (PKE) and magnetic linear dichroism (MLD) measured in (Ga,Mn)As epilayer with x = 5.2%, the arrow indicate the spectral position of the laser pulses used in the time-resolved experiment shown in Supplementary Figures S10 and S14; note that the data for MLD are multiplied by 5 for clarity.

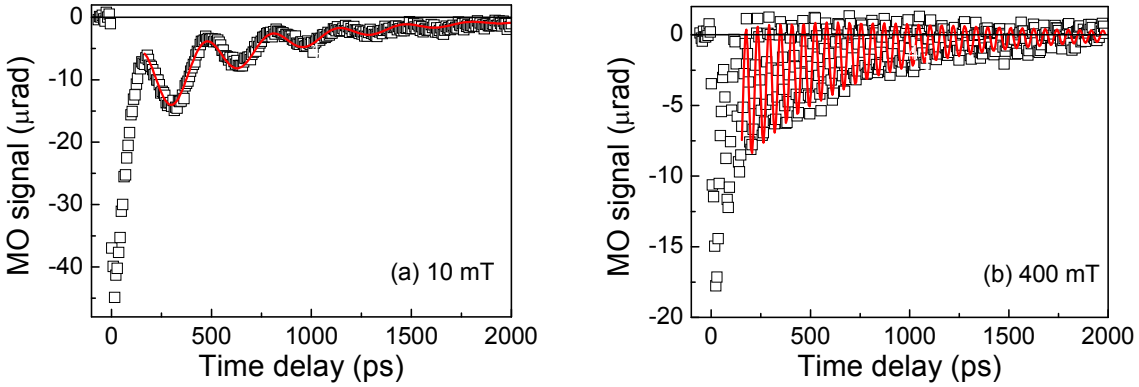

Supplementary Figure S14. **Evaluation of the Gilbert damping coefficient from magneto-optical (MO) signal damping.** Dynamics of the MO signal measured for external magnetic field $\mu_0 H_{ext}$ = 10 mT (a) and 400 mT (b) applied along the [010] crystallographic direction in (Ga,Mn)As epilayer x = 5.2% (points); lines are fits by Landau-Lifshitz-Gilbert equation.

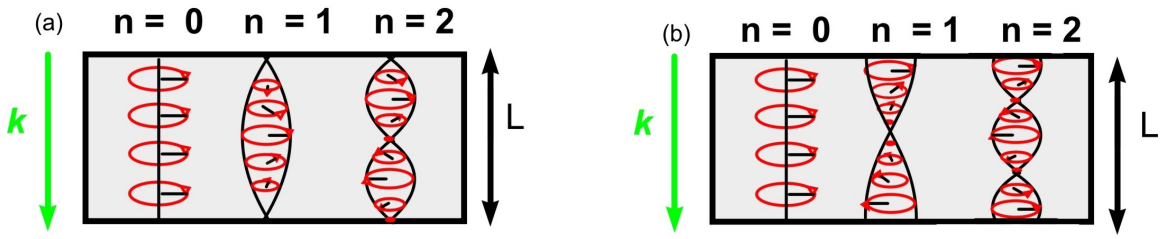

Supplementary Figure S15. **Schematic illustration of spin wave resonances.** In homogeneous thin magnetic films with a thickness L, only the perpendicular standing waves with a wave vector k fulfilling the resonant condition $kL = n\pi$ are amplified; n is the mode number. The mode with $n = 0$ denotes the uniform magnetization precession with zero k vector. In principle, there exist two symmetric boundary conditions that have a node (a) or maximum (b) at the surface.

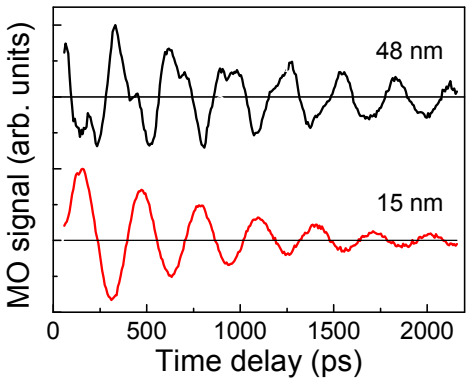

Supplementary Figure S16. **Appearance of spin wave resonances in measured magneto-optical (MO) signals.** Comparison of oscillatory parts of MO signals measured (for $\mu_0 H_{ext}$ = 20 mT applied along the [010] crystallographic direction) in the original 48 nm thick (Ga,Mn)As epilayer with x = 7% and in the epilayer that was etched down to 15 nm; the curves are normalized and vertically shifted for clarity. In the 15 nm thick epilayer only the uniform magnetization precession is observed while in the 48 nm thick epilayer three spin wave resonances can be identified (see Fig. 6(b) in the main paper for the corresponding FFT spectra).

Supplementary Note #1

(Ga,Mn)As as a model material for spintronic research

The achievement of ferromagnetism in an ordinary III-V semiconductor with Mn concentrations exceeding 1% demonstrates on its own the sensitivity of magnetic properties to doping. Several experiments have verified that changes in the carrier density and distribution in thin (III,Mn)As films due to an applied gate voltage can induce reversible changes of the Curie temperature T_c and other magnetic and magneto-transport properties.[54,61-66] Experiments in which ferromagnetism in a (III,Mn)As system is turned on and of optically or in which recombination of spin-polarized carriers injected from the ferromagnetic semiconductor yields emission of circularly polarized light clearly demonstrated the interplay between optoelectronics and magnetism in these materials.[67-69]

By exploiting the large spin polarization of carriers in (Ga,Mn)As and building on the well established heterostructure growth and microfabrication techniques in semiconductors, high quality magnetic tunnel junctions have been demonstrated showing large tunneling magnetoresistances.[70-73] In the studies of the inverse magneto-transport effects, namely spin-transfer torques in tunnel junctions[74] and domain walls,[75-80] the dilute-moment p-type (Ga,Mn)As is unique for its low saturation magnetization and strongly spin-orbit coupled valence band.[19,81,82] This implies low currents required to excite magnetization dynamics and the leading role of magnetocrystalline anisotropies over the dipolar shape anisotropy fields, which allows for unprecedented control of the magneto-transport phenomena ex situ by microfabrication[77,83] or in situ by piezo-electric gating.[84-86] Besides the more conventional spintronic effects based on the Mott's two-spin-channel model of conduction in ferromagnets, such as the tunneling magnetoresistance and spin transfer torque, (Ga,Mn)As studies have also focused on the other distinct type of spintronics phenomena based on the Dirac's spin-orbit coupling.[87,87] Here among the new effects discovered in (Ga,Mn)As, and subsequently observed in other systems including conventional metal magnets, are the anisotropic magnetoresistance in tunneling[89-91] and single-electron transport devices[87,92,93] and the spin-orbit current induced torque observed in uniform magnetic structures.[94-96] The optical activity of (Ga,Mn)As, characteristic of direct-gap semiconductors, has led to the discovery of the optical counterparts of the current induced torques.[40,59]

Supplementary Note #2

Theory of (Ga,Mn)As

The elements in the (Ga,Mn)As compound have nominal atomic structures [Ar]$3d^{10}4s^2p^1$ for Ga, [Ar]$3d^5 4s^2$ for Mn, and [Ar]$3d^{10}4s^2p^3$ for As. This circumstance correctly suggests that the most stable position of Mn in the GaAs host lattice, at least up to certain level of Mn doping, is on the Ga site where its two 4*s*-electrons can participate in crystal bonding in much the same way as the two Ga 4*s*-electrons. Because of the missing valence 4*p*-electron, the Mn_{Ga} impurity acts as an acceptor. In the electrically neutral state, the isolated Mn_{Ga} has the character of a local moment with zero angular momentum and spin S = 5/2 (Lánde g-factor g = 2) due to the five 3*d* electrons and a moderately bound hole. GaAs is an intermediate band-gap III-V semiconductor, with E_g = 1.5 eV at low temperatures. The experimental acceptor binding energy of an isolated Mn impurity substituting for Ga is of an intermediate strength, $E_a^0 \approx 0.1$ eV.[97-101]

The perturbation of the crystal potential of GaAs due to a single Mn impurity has three main components (see Supplementary Figure S1).[6] (i) The first is the long-range hydrogenic-like potential of a single acceptor in GaAs which produces a bound state at about 30 meV above the valence band.[102] (ii) The second contribution is a short-range central-cell potential. It is specific to a given impurity and reflects the difference in the electro-negativity of the impurity and the host atom.[103] For a conventional non-magnetic acceptor Zn_{Ga}, which is the 1st nearest neighbor of Ga in the periodic table, the atomic *p*-levels are shifted by ~0.25 eV which increases the binding energy by ~5 meV. For Mn, the 6th nearest neighbor of Ga, the *p*-level shift is ~1.5 eV which when compared to Zn_{Ga} implies the central-cell contribution to the acceptor level of Mn_{Ga} ~30 meV.[99] (iii) The remaining part of the Mn_{Ga} binding energy is due to the spin-dependent hybridization of Mn *d*-states with neighboring As *p*-states. Its contribution, which has been directly inferred from spectroscopic measurements of uncoupled Mn_{Ga} impurities,[99,104] is again comparable to the binding energy of the hydrogenic single-acceptor potential. Combining (i)-(iii) accounts for the experimental binding energy of the Mn_{Ga} acceptor of 0.1 eV. An important caveat to these elementary considerations is that the short-range potentials alone of strengths inferred in (ii) and (iii) would not produce a bound-state above the top of the valence band but only a broad region of scattering states inside the valence band.

The low-energy degrees of freedom in (Ga,Mn)As materials are the orientations of Mn local moments and the occupation numbers of acceptor levels near the top of the valence band. The number of local moments and the number of holes may differ from the number of

Mn_{Ga} impurities in the GaAs host due to the presence of charge and moment compensating defects. Hybridization between Mn *d*-orbitals and valence As/Ga *sp*-orbitals, mainly the As *p*-orbitals on the neighboring sites, leads to an antiferromagnetic exchange interaction between the spins that they carry.[5]

At concentrations << 1% of substitutional Mn, the average distance between Mn impurities (or between holes bound to Mn ions) is much larger than the size of the bound hole characterized approximately by the impurity effective Bohr radius. These very dilute (Ga,Mn)As systems are insulating, with the holes occupying a narrow impurity band, and paramagnetic. Experimentally, ferromagnetism in (Ga,Mn)As is observed when Mn doping reaches approximately 1% and the system is still below but near the insulator-to-metal transition.[25,105-107] (x = 1% Mn-doping corresponds to $N_{Mn} = 2.2\times10^{20}$ cm^{-3} in Ga_{1-x},Mn_xAs.) At these Mn concentrations, the localization length of the holes is extended to a degree that allows them to mediate, via the *sp* - *d* hybridization, ferromagnetic exchange interaction between Mn local moments, even though the moments are dilute.

Beyond a critical Mn doping, which in experiments is about 1.5%, Mn doped GaAs exhibits a phase transition to a state in which the Mn impurity levels overlap sufficiently strongly that the ground state is metallic, i.e., that states at the Fermi level are not bound to a single or a group of Mn atoms but are delocalized across the system.[5,107,108] In the metallic regime Mn can, like a shallow acceptor (C, Be, Mg, Zn, e.g.), provide delocalized holes with a low-temperature density comparable to Mn density, N_{Mn}.[53,109,110] The transition to the metallic state occurs at N_{Mn} which is about two orders of magnitude larger than in GaAs doped with shallow acceptors.[111] This is because of the central cell and *pd*-hybridization contributions to the binding energy which makes Mn acceptors more localized than the shallow acceptors. A crude estimate of the critical metal-insulator transition density can be obtained with a short-range potential model, using the experimental binding energy and assuming an effective mass of valence band holes, $m^* = 0.5m_e$. This model implies an isolated acceptor level with effective Bohr radius $a_0 = (\hbar^2 / 2m^* E_a^0)^{1/2} = 1$ nm. The radius a_0 then equals the Mn impurity spacing scale $N_{Mn}^{-1/3}$ at $N_{Mn} \approx 10^{21}$ cm^{-3}. This explains qualitatively the higher metal-insulator-transition critical density in Mn doped GaAs compared to the case of systems doped with shallow, more hydrogenic-like acceptors which have binding energies $E_a^0 \approx 30$ meV.[101,111]

Unlike the metal-insulator phase transition, which is sharply defined in terms of the temperature $T = 0$ limit of the conductivity, the crossover in the character of states near the

Fermi level in semiconductors with increased doping is gradual.[5,112-115] At very weak doping, the Fermi level resides inside a narrow impurity band (assuming some compensation) separated from the valence band by an energy gap of a magnitude close to the impurity binding energy. In this regime strong electronic correlations are an essential element of the physics and a single-particle picture has limited utility. Well into the metallic state, on the other hand, the impurities are sufficiently close together, and the long-range Coulomb potentials which contribute to the binding energy of an isolated impurity are sufficiently screened, that the system is best viewed as an imperfect crystal with disorder-broadened and shifted host Bloch bands. In this regime, electronic correlations are usually less strong and a single-particle picture often suffices. (Note that the short-range components of the Mn binding energy in GaAs, which are not screened by the carriers, move the crossover to higher dopings and contribute significantly to carrier scattering in the metallic state.)

Although neither picture is very helpful for describing the physics in the crossover regime which spans some finite range of dopings, the notion of the impurity band on the lower doping side from the crossover and of the disordered host band on the higher doping side from the crossover still have a clear qualitative meaning. The former implies that there is a deep minimum in the density-of-states between separate impurity and host band states. In the latter case the impurity band and the host band merge into one inseparable band whose tail may still contain localized states depending on the carrier concentration and disorder. Note that terms overlapping and merging impurity and valence bands describe the same basic physics in (Ga,Mn)As. This is because the Mn-acceptor states span several unit cells even in the very dilute limit and many unit cells as the impurity band broadens with increasing doping. The localized and the delocalized Bloch states then have a similarly mixed As-Ga-Mn *spd*-character. This applies to systems on either side of the metal-insulator transition.

The picture of ferromagnetism in (Ga,Mn)As mediated by holes in the exchange-split disordered valence band builds on the above picture of the Mn_{Ga} acceptor in which the presence of the long-range hydrogenic-like impurity potential is essential for creating a bound state in the band gap; with increasing doping, the impurity level broadens and for a sufficiently screened hydrogenic potential the impurity states merge into the valence band. A microscopic theory most closely related to these considerations is based on the *spd* tight-binding approximation (TBA) Hamiltonian of (Ga,Mn)As in which electronic correlations on the localized Mn *d*-orbitals are treated using the Anderson model of the magnetic impurity and disorder is treated within the coherent potential approximation (CPA) or by supercell calculations.[6] In Supplementary Figure S2 we plot an examples of the total and orbital

resolved densities of states (DOSs) for 10% Mn_{Ga} impurities. The Mn-*d* spectral weight is peaked at approximately 4 eV bellow the top of the valence band, in agreement with photoemission data,[64] and is significantly smaller near the Fermi energy E_F . The Fermi level states at the top of the valence band have a dominant As(Ga) *p*-orbital character. The *p-d* coupling strength, $N_0\beta = \Delta/(Sx)$,[5] determined from the calculated valence band exchange splitting Δ (and taking $S = 5/2$) is close to the upper bound of the reported experimental range of $N_0\beta$ ~1-3 eV.[99,116-119] This is regarded as a moderately weak *p-d* coupling because the corresponding Fermi level states of the (Ga,Mn)As have a similar orbital character as the states in the host GaAs valence band. These spectral features are among the key characteristics of the hole mediated ferromagnetism in (Ga,Mn)As.

The model effective Hamiltonian theory of (Ga,Mn)As, based on the $\boldsymbol{k}\cdot\boldsymbol{p}$ kinetic-exchange (Zener) approximation,[5,120,121] assumes a value of $N_0\beta$ also within the range of 1-3 eV (typically closer to the lower experimental bound.[5]) It is this moderate *p-d* hybridization that allows it to be treated perturbatively and to perform the Schrieffer-Wolf transformation from the microscopic TBA-Anderson Hamiltonian to the effective model in which valence band states experience a spin-dependent kinetic-exchange field.[5] Hence, the effective kinetic-exchange model and the microscopic TBA theory provide a consistent physical picture of ferromagnetic (Ga,Mn)As. In Supplementary Figure S3 we show DOSs over the entire Mn_{Ga} doping range obtained from the LDA+U density functional calculations.[6,122] The LDA+U, the TBA, and the kinetic-exchange Zener theories all provide a compatible picture of the band structure of ferromagnetic (Ga,Mn)As. Simultaneously, it is important to keep in mind that the moderate acceptor binding energy of Mn_{Ga} shifts the insulator-to-metal transition to orders of magnitude higher doping densities than in the case of common shallow non-magnetic acceptors.[6,107] Disorder and correlation effects, therefore, play a comparatively more significant role in (Ga,Mn)As than in degenerate semiconductors with common shallow dopants and any simplified one-particle band picture of ferromagnetic (Ga,Mn)As can only represent a proxy to the electronic structure of the material.

Since the bands evolve continuously from the intrinsic non-magnetic semiconductor GaAs, via the degenerate ferromagnetic semiconductor (Ga,Mn)As to the ferromagnetic metal MnAs, it can by expected that T_c of MnAs (with the value close to room temperature) sets the upper theoretical bound of achievable T_c's across the entire doping range. In experiment, as we show below, the Mn_{Ga} doping is limited to approximately 10% with corresponding T_c reaching 190 K in uniform thin-film crystals prepared by optimized low-temperature epitaxy

synthesis and post-growth annealing. In these samples the hole density is already in the 10^{21} cm^{-3} range, i.e., closer to typical metal carrier densities rather then densities in commonly used non-magnetic semiconductor. The motivation to push T_c higher by forcing the GaAs host to accept more substitutional Mn_{Ga} impurities is, therefore, not particularly strong. It will unlikely reach values suitable for room-temperature applications and simultaneously the doping will become to high to allow for suitable electrostatic gating effects. On the other hand, (Ga,Mn)As can be regarded as a well behaved and understood degenerate semiconductor and band ferromagnet and as a particularly useful test-bed model system for many lines of spintronics research.

Finally we note that, narrow impurity bands have been clearly observed in Mn doped GaAs samples with carrier densities much lower than the metal-insulator transition density, for example in equilibrium grown bulk materials with N_{Mn} = 10^{17} - 10^{19} cm^{-3}.[98,123,124] The energy gap between the impurity band and the valence band, E_a, can be measured by studying the temperature dependence of longitudinal and Hall conductivities, which show activated behavior because of thermal excitation of holes from the impurity band to the much more conductive valence band.[98,102,124] The activation energy decreases with increasing Mn density, following roughly the form[98] $E_a = E_a^0[1-(N_{Mn}/N_{Mn}^c)^{1/3}]$. The lowering of impurity binding energies at larger N_{Mn}, which is expected to scale with the mean impurity separation as expressed above, is apparent already in the equilibrium grown bulk materials with N_{Mn} = 10^{17} - 10^{19} cm^{-3}. The degenerate semiconductor regime was, however, not reached in the bulk materials. A comprehensive experimental assessment of basic doping trends including the regimes near and above the insulator-to-metal transition became possible since late 1990's with the development of epitaxial (Ga,Mn)As films which can be doped well beyond the equilibrium Mn solubility limit while avoiding phase segregation and maintaining a high degree of uniformity. [4,11,15,56,107]

Supplementary Note #3

Experiments preceding our determination of micromagnetic parameters of (Ga,Mn)As

Magnetic anisotropy fields, Gilbert damping constant and spin-stiffness are the basic parameters of a ferromagnet which determine its micromagnetic properties. The anisotropy fields are associated with the energy required to coherently rotate magnetic moments of the entire ferromagnet. They can be determined in a straightforward way in magnetization or magneto-transport measurements from external magnetic fields required to reorient the

magnetization of a ferromagnetic sample, or in magnetization dynamics experiments from the field-dependent resonant frequencies.[20,29,125,126]

Gilbert damping characterizes dissipative processes that drive the magnetization motion towards an equilibrium state. This phenomenon is usually investigated by the frequency-domain-based ferromagnetic resonance (FMR) experiment where the phenomenological Gilbert damping coefficient α is deduced from the resonance peak linewidth.[20,126] The experimentally measured FMR linewidths contain not only the frequency-dependent linewidth due to the Gilbert damping but also the frequency-independent inhomogeneous linewidth broadening.[20,126] To separate them, it is necessary to measure the linewidths at several microwave frequencies.[20,126] In FMR these frequencies are given by the resonant-cavity frequency that significantly complicates the frequency change. Therefore, the experiments are usually performed at only two different frequencies (typically, 9 and 35 GHz)[20] that makes the corresponding separation of the individual components in the measured signal rather questionable. Alternatively, α can be determined from the time-domain based magneto-optical pump-and-probe experiment by fitting the damping of the measured oscillatory data by Landau-Lifshitz-Gilbert equation.[34,127] However, to obtain the Gilbert damping coefficient from the measured value of α it is necessary to take into account a realistic magnetic anisotropy of the investigated samples (see below). Moreover, also the frequency dependence of α has to be measured for a separation of the intrinsic value of the Gilbert damping coefficient from the inhomogeneous parts of α. The absence of these two requirements and the un-optimized magnetic properties of the investigated samples led to a large scatter in the deduced values of α for $Ga_{1-x}Mn_xAs$ with a different Mn content x: The increase of α from ≈ 0.02 to ≈ 0.08 for the increase of x from 3.6% to 7.5% was reported in Ref. 34. On the contrary, in Ref. 127 the values of α from 0.06 to 0.19 – without any apparent doping trend – were observed for x from 2% to 11%.

The spin-stiffness is associated with the exchange energy of non-uniform local directions of the magnetization, in particular with the energy of small wave-vector spin-wave excitations of the ferromagnet. Considering a specific model of thermodynamic properties of the studied ferromagnet, the spin-stiffness can be indirectly inferred from the measured temperature dependence of magnetization,[25] Curie temperature,[25] or domain wall width.[26] The direct determination of the spin-stiffness from magnetization dynamics experiments is significantly more challenging than in the case of the magnetic anisotropy fields.[21-24,27] The low-energy non-uniform collective excitations of the system can be strongly affected by

inhomogeneities or surface properties of the ferromagnet for which specific models have to be assumed in order to extract the spin-stiffness constant from the measured data. An exception are the Kittel spin-wave modes of a uniform thin-film ferromagnet for which the spin-stiffness parameter D is directly obtained from the measured resonant fields (see below). To date, spin-wave resonance measurements of (Ga,Mn)As have been reported on > 100 nm thick epilayers.[21-24] The Kittel modes with $\Delta H_n \sim n^2$ were observed only in a 120 nm thick, 8% Mn doped (Ga,Mn)As for magnetic fields applied close to the magnetic easy-axis.[23] Measurements of the same sample in other field orientations showed different trends which indicated the presence of strong inhomogeneities and surface dependent effects.[23] A non-Kittel-like linear or sublinear dependence of the resonant fields on the mode index has been reported also in the other ferromagnetic resonance measurements of thick (Ga,Mn)As epilayers.[21-24] In complementary studies of the magnetization dynamics induced and detected by magneto-optical pump-and-probe measurements, only two resonant frequencies were identified.[27] Based on the theoretical modeling, they were not ascribed to the Kittel modes but rather to coupled bulk-surface modes which again made the extraction of the spin-stiffness constant dependent on the considered model of bulk and surface properties of the studied sample.[27] The extracted values of the spin-stiffness from all available magnetic resonance data in (Ga,Mn)As materials, complemented by values inferred from magnetization and domain studies,[25,26] are scattered over more than an order of magnitude and show no clear trend as a function of Mn-doping or other material parameters of the (Ga,Mn)As ferromagnetic semiconductor.[28]

In this Supplementary Information we show how we are able to deduce from a *single* magneto-optical pump-and-probe experiment all these micromagnetic parameters. In particular, the anisotropy fields can be determined from the dependence of the precession frequency on the external magnetic filed combined with the probe-polarization dependence of the precession signal amplitude. The Gilbert damping constant can be deduced from the precession signal damping. Finally, the spin stiffness can be obtained from the mutual spacing of the precession modes which are present in the measured oscillatory magneto-optical signal.

Supplementary Note #4

Evaluation of hole concentration

In Supplementary Figure S4 we show results of the Hall effect measurements at 4.2 K. For this purpose the samples were lithographically patterned into Hall-bars of 60 μm width. It can be seen in the figure that the Hall signal is affected by longitudinal magnetoresistance R_{xx} of the samples, especially at low dopings. Therefore,

$$R_{xy} = B/(epd) + k_1 R_{xx} + k_2 R_{xx}^2 \quad \text{(S1)}$$

where d is the sample thickness and k_1 and k_2 are fitting constants reflecting the anomalous Hall effect and possible imperfections in the geometry of the Hall bars. We also emphasize that, apart from the common experimental scatter and from the corrections due to the non-zero magnetoresistance and due to the anomalous Hall effect, the carrier density can in principle be inferred only approximately from the slope of the Hall curve in a multi-band, spin-orbit coupled exchange-split system such as the (Ga,Mn)As. The error bar due to the multi-band nature is estimated to be ≈ 20%.[110] Due to these uncertainties we can only make semi-quantitative conclusions based on the measured Hall effect hole densities.

Supplementary Note #5

Evaluation of epilayer thickness

For an evaluation of material parameters from an experimentally measured data (e.g., for an evaluation of the hole densities from the measured transversal resistances which is described above) it is necessary to know the (Ga,Mn)As epilayer thicknesses. However, accurate determination of layer thicknesses is a nontrivial task in case of thin (Ga,Mn)As layers. Some standard techniques (e.g., X-ray reflectivity or optical ellipsometry) are inapplicable due to the weak contrast between the (Ga,Mn)As layer and the GaAs substrate, or unknown optical parameters. The relative accuracy of other common techniques (e.g., of X-ray diffraction) does not exceed 10% because of the small thickness of the measured layer. Therefore, we used a thickness estimation based on the following quantities: (i) the growth time and the growth rate of the GaAs buffer layer measured by the RHEED oscillations (typical accuracy of ±3%); (ii) increase in the growth rate by adding the known Mn-flux measured by the beam-flux monitor relatively to the Ga flux (typical accuracy of ±5% of the Mn vs. Ga flux ratio); (iii) reduction of thickness by the native oxidation (-1.5 nm ± 0.5 nm); (iv) reduction of thickness by thermal oxidation (-1.0 nm ± 0.5 nm). Relative accuracy of steps (i) and (ii) was verified on separate calibration growths of (Ga,Mn)As on AlAs, where

an accurate X-ray reflectivity method to measure the (Ga,Mn)As layer thickness could be used. Typical thicknesses of the native and the thermal oxides in steps (iii) and (iv) were determined by XPS. The resulting total accuracy of the (Ga,Mn)As layer thickness determination is thus 3% (relative random error) and 1 nm (systematic error).

Supplementary Note #6

Analytical description of magnetization dynamics in (Ga,Mn)As

The dynamics of magnetization is described by the Landau-Lifshitz-Gilbert (LLG) equation. We used LLG equation in spherical coordinates where the time evolution of magnetization magnitude M_s and orientation, which is characterized by the polar θ and azimuthal φ angles, is given by:

$$\frac{dM_s}{dt} = 0 \ , \tag{S2}$$

$$\frac{d\theta}{dt} = -\frac{\gamma}{\left(1+\alpha^2\right)M_s}\left(\alpha \cdot A + \frac{B}{\sin\theta}\right), \tag{S3}$$

$$\frac{d\varphi}{dt} = \frac{\gamma}{\left(1+\alpha^2\right)M_s \sin\theta}\left(A - \frac{\alpha \cdot B}{\sin\theta}\right), \tag{S4}$$

where α is the Gilbert damping coefficient. The gyromagnetic ratio $\gamma = \left(g\mu_B\right)/\hbar$, where $g = 2$ is the Landé g-factor of Mn moments, μ_B the Bohr magneton, and $\hbar$ is the reduced Planck constant. Functions $A = dF/d\theta$ and $B = dF/d\varphi$ are the derivatives of the energy density functional F with respect to θ and φ, respectively. We expressed F in a form:[29]

$$F = M\left[\begin{array}{l} K_c \sin^2\theta\left(\frac{1}{4}\sin^2 2\varphi \sin^2\theta + \cos^2\theta\right) - K_{out}\cos^2\theta - \frac{K_u}{2}\sin^2\theta\left(1-\sin 2\varphi\right) - \\ - H_{ext}\left[\cos\theta\cos\theta_H + \sin\theta\sin\theta_H\cos\left(\varphi-\varphi_H\right)\right] \end{array}\right], \tag{S5}$$

where K_c, K_u and K_{out} are constants that characterize the cubic, uniaxial and out-of-plane magnetic anisotropy fields in (Ga,Mn)As, respectively, and H_{ext} is the external magnetic field whose orientation is given by the angles θ_H and φ_H. For a small deviations $\delta\theta$ and $\delta\varphi$ from the equilibrium values θ_0 and φ_0, the solution of Supplementary Equations S3 and S4 can be written in a form

$$\theta(t) = \theta_0 + A_\theta e^{-k_D t}\cos(2\pi f t + \Phi_\theta), \tag{S6}$$

$$\varphi(t) = \varphi_0 + A_\varphi e^{-k_D t}\cos(2\pi f t + \Phi_\varphi), \tag{S7}$$

where the constants A_θ (A_φ) and Φ_θ (Φ_φ) describe the initial amplitude and phase of θ (φ), respectively. The precession frequency f and oscillation damping rate k_D are given by

$$f = \frac{g\mu_B}{h\left(1+\alpha^2\right)}\sqrt{\begin{array}{l}\left(H_{ext}\cos(\varphi-\varphi_H) - 2K_{out} + \frac{K_c(3+\cos 4\varphi)}{2} + 2K_u\sin^2\left(\varphi-\frac{\pi}{4}\right)\right)\times \\ \times\left(H_{ext}\cos(\varphi-\varphi_H) + 2K_c\cos 4\varphi - 2K_u\sin(2\varphi)\right) + \\ +\alpha^2\left\{\begin{array}{l}\left(H_{ext}\cos(\varphi-\varphi_H) - 2K_{out} + \frac{K_c}{2}(3+\cos 4\varphi) + 2K_u\sin^2\left(\varphi-\frac{\pi}{4}\right)\right)\times \\ \times\left(H_{ext}\cos(\varphi-\varphi_H) + 2K_c\cos 4\varphi - 2K_u\sin(2\varphi)\right) - \\ \left(H_{ext}\cos(\varphi-\varphi_H) - K_{out} + 2K_c\frac{1}{8}(3+5\cos 4\varphi) + \frac{K_u}{2}(1-3\sin(2\varphi))\right)^2\end{array}\right\}\end{array}}, \tag{S8}$$

$$k_D = \alpha\frac{g\mu_B}{2\hbar\left(1+\alpha^2\right)}\left(2H_{ext}\cos(\varphi-\varphi_H) - 2K_{out} + \frac{K_c}{2}(3+5\cos 4\varphi) + K_u(1-3\sin(2\varphi))\right). \tag{S9}$$

In our case, the investigated (Ga,Mn)As epilayers are in-plane magnets (i.e., $\theta \approx \pi/2$), the external magnetic field is applied in the sample plane (i.e., $\theta_H \approx \pi/2$), and the precession damping is relatively slow (i.e., $\alpha^2 \approx 0$) which yields

$$f = \frac{g\mu_B}{h}\sqrt{\begin{array}{l}\left(H_{ext}\cos(\varphi-\varphi_H) - 2K_{out} + \frac{K_c(3+\cos 4\varphi)}{2} + 2K_u\sin^2\left(\varphi-\frac{\pi}{4}\right)\right)\times \\ \times\left(H_{ext}\cos(\varphi-\varphi_H) + 2K_c\cos 4\varphi - 2K_u\sin(2\varphi)\right)\end{array}}, \tag{S10}$$

$$k_D = \alpha\frac{g\mu_B}{2\hbar}\left(2H_{ext}\cos(\varphi-\varphi_H) - 2K_{out} + \frac{K_c}{2}(3+5\cos 4\varphi) + K_u(1-3\sin(2\varphi))\right). \tag{S11}$$

Supplementary Equation S10 express the sensitivity of the magnetization precession frequency to the magnetic anisotropy of the material that is a well-known effect which form the basis for the interpretation of FMR.[126] More interestingly, Supplementary Equation S11

shows that the precession damping k_D, which is measured experimentally, depends not only on the Gilbert damping parametr α but also on the sample anisotropy and on the mutual orientation of the external magnetic field and the magnetization.

We note that in previously reported magneto-optical pump-and-probe experiments[33,34,37-39, 127,128] the measured experimental data were modeled by LLG equation in the form

$$\frac{d\vec{M}(t)}{dt} = -\gamma\left[\vec{M}(t)\times\vec{H}_{eff}(t)\right] + \frac{\alpha}{M_s}\left[\vec{M}(t)\times\frac{d\vec{M}(t)}{dt}\right], \tag{S12}$$

where $\boldsymbol{H_{eff}}$ is the effective magnetic field. However, in (Ga,Mn)As the magnetic anisotropy is rather complex and, therefore, modeling of MO signals by LLG in this form does not provide realistic values of α because it is not possible to disentangle the effect of magnetic anisotropy from α (see Supplementary Equation S11). We believe that this is one of the reasons why the dependence of α on Mn concentration was so different in Ref. 34 and Ref 127. Similarly, the change of magnetic anisotropy of (Ga,Mn)As during the deposition of metal overlayer could be partially responsible for the changes of α that were reported in Ref. 39.

Supplementary Note #7

Evaluation of magnetic anisotropy

The dependence of the precession frequency on the magnetic anisotropy fields and on the magnitude and orientation of external magnetic field (cf. Supplementary Equation S10) enables to evaluate the magnetic anisotropy from the experimentally measured precession frequencies very similarly as in the case of FMR.[126] In particular, for a sufficiently strong external magnetic field $\varphi = \varphi_H$ and the following equations can be used to fit the precession frequencies measured

a) for H_{ext} along the [110] crystallographic direction (i.e., $\varphi_H = \pi/4$):

$$f = \frac{g\mu_B}{h}\sqrt{\left(H_{ext} - 2K_{out} + K_c\right)\left(H_{ext} - 2K_c - 2K_u\right)} \tag{S13}$$

b) for H_{ext} along the [010] crystallographic direction (i.e., $\varphi_H = \pi/2$):

$$f = \frac{g\mu_B}{h}\sqrt{\left(H_{ext} - 2K_{out} + 2K_c + K_u\right)\left(H_{ext} + 2K_c\right)} \tag{S14}$$

c) for H_{ext} along the [-110] crystallographic direction (i.e., $\varphi_H = 3\pi/4$):

$$f = \frac{g\mu_B}{h}\sqrt{\left(H_{ext} - 2K_{out} + K_c + 2K_u\right)\left(H_{ext} - 2K_c + 2K_u\right)} \qquad \text{(S15)}$$

As an example, in Supplementary Figure S9 we show the measured dependences $f(H_{ext})$ and their fits for two orientations of H_{ext}. To increase the precision of the magnetic anisotropy determination even further, for all the investigated samples we supplemented this method by two additional experimental techniques that provide information about the samples magnetic anisotropy – namely, the probe-polarization dependence of the MO precession signal amplitude and SQUID magnetometry.

In (Ga,Mn)As there are two MO effects that are responsible for the measured rotation of the polarization plane $\Delta\beta$ of the reflected linearly polarized light at normal incidence.[41] The first of the MO effects is the well-known polar Kerr effect (PKE), where $\Delta\beta$ occurs due to the different index of refraction for σ^+ and σ^- circularly polarized light propagating parallel to the direction of magnetization $\boldsymbol{M}$. The polarization rotation due to PKE is proportional to the projection of magnetization to the direction of light propagation, it is linear in magnetization (i.e., its sign is changed when the direction of magnetization is reversed), and it is independent on the orientation of the input linear polarization β (see Supplementary Figure S10(b) for the angle definition).[41] The second MO effect is the magnetic linear dichroism (MLD), which originates from different absorption (reflection) coefficient for light linearly polarized parallel and perpendicular to $\boldsymbol{M}$, that occurs if the light propagates perpendicular to the direction of magnetization $\boldsymbol{M}$. The polarization rotation due to MLD is proportional to the projection of magnetization to the direction perpendicular to the direction of light propagation, it is quadratic in magnetization (i.e., its sign is not changed when the direction of magnetization is reversed) and it varies as $\sin(2\beta)$.[41] In Supplementary Figure S10(a) we show the MO signals measured by probe pulses with different orientations β for identical pumping conditions. The measured dynamical MO signal δMO, which is a function of the time delay between pump and probe pulses Δt and the probe polarization orientation β, can be fitted well by the phenomenological equation,[41]

$$\delta MO(\Delta t, \beta) = A(\beta)\cos\left[2\pi f \Delta t + \Phi(\beta)\right]e^{-\Delta t/\tau_G} + C(\beta)e^{-\Delta t/\tau_p}, \qquad \text{(S16)}$$

where A and C are the amplitudes of the oscillatory and pulse function, respectively, f is the ferromagnetic moment precession frequency, Φ is the phase factor, τ_G is the Gilbert damping time, and τ_p is the pulse function decay time. All the measured data in Supplementary Figure S10(a) can be fitted well by Supplementary Equation S16 with a one set of parameters f, τ_G and τ_p. The dependence $A(\beta)$ obtained by this fitting procedure is displayed in Supplementary Figure S10(c). The position of the maximum in the dependence $A(\beta)$ at $\beta \approx 120°$ corresponds to the equilibrium position of the easy axis in the sample - i.e., the in-plane position of magnetization without the pump pulse φ_0.[41] The position of the easy axis in the sample plane is given by the relative magnitude of the cubic (K_c) and uniaxial (K_u) anisotropy fields. Therefore, by measuring φ_0 without external magnetic field applied, we are directly measuring the ratio K_c / K_u.

The in-plane anisotropy constants can be obtained also from magnetization loops measured by SQUID magnetometry. For any external magnetic field the orientation of magnetization is determined by the minimum of the energy (cf. Supplementary Equation S5). If the orientation of magnetization as function of external magnetic field is known, the projection of the magnetization into the measurement axis can be easily numerically evaluated for every point of the magnetization loop. To obtain the anisotropy constants, we fitted the experimental data measured by SQUID until we obtained the best agreement between the data and the calculated magnetization – see Supplementary Figure S11. It is worth noting that this model does not describe the switching mechanism (governed by the domain wall physics which is not treated in our single domain description), so the parts of hysteresis loops containing the switching were not used in the analysis. Moreover, in the case of uniaxial systems ($K_u > K_c$) an analytical expression for the magnetization measured along the hard axis can be utilized to analyze the data.[125]

To sum up, by a simultaneous fitting of the measured dependence of the precession frequency on an external magnetic field (Supplementary Figure S9), of the MO signal precession amplitude on a probe-polarization [Supplementary Figure S10(c)], and of the data measured by SQUID magnetometry (Supplementary Figure S11) we evaluated very precisely the magnetic anisotropy for all the investigated samples. The example of the obtained in-plane angular dependence of the free energy in (Ga,Mn)As epilayer with Mn concentration x = 5.2% is shown in Supplementary Figure S12.

Supplementary Note #8

Determination of Gilbert damping coefficient

For numerical modeling of the measured MO data, we first computed from the LLG equation (Supplementary Equations S3 and S4 with the measured magnetic anisotropy fields) the time-dependent deviations of the spherical angles [$\delta\theta(t)$ and $\delta\varphi(t)$] from the corresponding equilibrium values (θ_0, φ_0). Then we calculated how such changes of θ and φ modify the static magneto-optical response of the sample MO^{stat}, which is the signal that we detect experimentally:[41]

$$\delta MO(\Delta t,\beta) = -\delta\theta(\Delta t)P^{PKE} + \delta\varphi(\Delta t)P^{MLD}2\cos 2(\varphi_0-\beta) + \frac{\delta M_s(\Delta t)}{M_0}P^{MLD}2\sin 2(\varphi_0-\beta). \quad \text{(S17)}$$

The first two terms in Supplementary Equation S17 are connected with the out-of-plane and in-plane movement of magnetization, and the last term describes a change of the static magneto-optical response of the sample due to the laser-pulses induced demagnetization.[41] P^{PKE} and P^{MLD} are MO coefficients that describe the MO response of the sample which we measured independently in a static MO experiment for all the samples – see Supplementary Figure S13 for MO spectra measured in sample with x = 5.2%.

Examples of the fitting of the dynamical MO optical data are shown in parts (a) and (b) of the Supplementary Figure S14. The measured data can be fitted well by LLG for time delays longer than ≈ 150 ps, which is a time that it takes to establish the quasi-equilibrium conditions in the sample. We stress that the only fitting parameters in our modeling are the damping coefficient α, the initial deviation of the spherical angles from the corresponding equilibrium values, and the parameters describing the in-plane movement of the easy axis and the demagnetization signal, which are apparent as the non-oscillatory signal in the measured dynamics.[41] The obtained dependence of α on H_{ext} is shown in Fig. 5(c) in the main paper for two different orientations of H_{ext}. For H_{ext} applied along the [010] direction, α decreases monotonously with H_{ext}. On the contrary, for H_{ext} applied along [110] direction, α is a non-monotonous function of H_{ext} reaching a similar values of α for 0 mT and 100 mT. However, this non-monotonous dependence is a consequence of the field-induced frequency decrease (see Supplementary Figure S9) when the magnetic field is applied along the magnetically hard [110] direction (see Supplementary Figure S12). When α is plotted as a function of the

precession frequency (rather than the external field) we do not observe any significant difference between the different crystallographic directions – see Fig. 5(d) in the main paper. A field dependent damping parameter was reported in various magnetic materials and a variety of underlying mechanisms responsible for it were suggested as an explanation.[12,13,129-131] In our case, the most probable explanation seems to be the one that was used by Walowski *et al.* to explain the experimental results obtained in thin films of nickel.[12] They argued that in the low field range small magnetization inhomogeneities can be build – the magnetization does not align parallel in an externally applied field, but forms ripples.[12] Consequently, the measured MO signal, which detects sample properties averaged over the laser spot size, experiences an apparent oscillation damping α because the magnetic properties (i.e., the precession frequencies) are slightly differing within the spot size (see Fig. 6 and 7. in Ref. 12). On the other hand, for stronger external fields the sample is fully homogeneous and, therefore, the precession damping is not dependent on the applied field as expected for the intrinsic Gilbert damping coefficient.[132-136]

Supplementary Note #9

Determination of spin stiffness

We observed more than one precession mode in (Ga,Mn)As epilayers with a sufficient thickness. These precession modes are the spin wave resonances (SWRs) – i.e., spin waves (or magnons) that are selectively amplified by fulfilling the boundary conditions of the thin magnetic film.[60,136] Up to now, SWRs in (Ga,Mn)As were investigated mainly in a frequency-domain where they are apparent as multiple absorption peaks in the FMR spectra.[22-24,126] The existence of multiple resonances in FMR reveal that there exist several external magnetic fields at which the Larmor precession frequency in the sample coincides with the microwave frequency. The resonant field for the n-th mode (H_n) is obtained by solving the LLG equation with a term corresponding to exchange interactions in the material and by considering the appropriate boundary condition.[23] In homogeneous thin films with a thickness L, only the perpendicular standing waves with a wave vector k fulfilling the resonant condition $kL = n\pi$ are amplified; the mode with $n = 0$ denotes the uniform magnetization precession with zero k vector. In principle, there exist two symmetric boundary conditions which are schematically illustrated in Supplementary Figure S15. The position of n-th SWR mode in the FMR spectrum H_n is given by the Kittel relation[23] and the following equation applies

$$\Delta H_n \equiv H_0 - H_n = n^2 \frac{D}{g\mu_B}\frac{\pi^2}{L^2} \ , \tag{S18}$$

where n is an integer, D is the exchange spin stiffness constant, μ_B is the Bohr magneton, g is the g-factor, and L is the sample thickness. In FMR only the modes with odd n are observed[23] and the corresponding resonant fields are smaller than that of the uniform magnetization precession (i.e., $\Delta H_n > 0$). In the magneto-optical pump-and-probe experiment, the external magnetic field is kept constant during the measurement of any dynamical MO trace. Consequently, the SWRs are apparent as additional frequencies that are larger than that of the uniform magnetization precession. Ultrafast optical pulses also excite all resonant modes without any k selectivity.[60,136] Consequently, for a homogeneous magnetic film with a given thickness, a higher number of SWRs is detectable in the MO dynamical traces than in the FMR spectra. This is particularly important for (Ga,Mn)As that is magnetically homogeneous only when prepared in a form of rather thin films and, therefore, where only a limited number of SWRs is present within a detectable range of the precession frequencies. For an external magnetic field H_{ext} applied in the sample plane, the angular frequency of the n-th SWR mode f_n is given by[126,137]

$$f_n = \frac{g\mu_B}{h}\sqrt{\left(H_{ext}\cos(\varphi-\varphi_H) - 2K_{out} + \frac{K_c(3+\cos 4\varphi)}{2} + 2K_u \sin^2\left(\varphi-\frac{\pi}{4}\right) + \Delta H_n\right)\times} \\ \sqrt{\times\left(H_{ext}\cos(\varphi-\varphi_H) + 2K_c\cos 4\varphi - 2K_u\sin(2\varphi) + \Delta H_n\right)} \ , \tag{S19}$$

which enables to convert the experimentally measured frequency spacing of individual modes to the field differences ΔH_n from which the magnitude of the spin stiffness D can be evaluated using Supplementary Equation S18 (see Fig. 6 in the main paper).

As we illustrate in the following chapter, the magnetic homogeneity of the investigated epilayer is absolutely essential for a correct determination of D from the measured SWR spacing. Therefore, the experimental results obtained in samples that had been prepared by etching the original 48 nm thick (Ga,Mn)As epilayer down to the thickness 39, 29 and 15 nm are of fundamental importance. In Fig. 6(b) in the main paper we show the corresponding FFT spectra of the measured oscillatory MO signals. Clearly, the frequency f_0 of the lowest SWR does not depend on the film thickness. This confirms that the lowest

observed SWR really corresponds to the uniform precession of magnetization and, moreover, it proves that this film is magnetically homogeneous. Also the spacing ΔH_1 shows the expected (see Supplementary Equation S18) linear dependence on n^2 and $1/L^2$ (see Fig. 6 in the main paper) that enables a reliable determination of the value of D. In Supplementary Figure S16 we compare the experimental data for 48 nm and 15 nm thick epilayers from which the FFT spectra depicted in Fig. 6(b) in the main paper were computed. Clearly, the etching of the sample from 48 nm to 15 nm not only suppressed the higher SWRs, which is apparent from the purely sinusoidal shape of the data for the 15 nm film, but it also increased the precession damping, which is probably a consequence of a slight variation of the etched film thickness within the laser spot size of 25 μm. These data illustrate that the magneto-optical pump-and-probe experiment is a very sensitive diagnostic tool not only of the magnetic but also of the structural quality of thin magnetic films.

Supplementary Note #10

Demonstration of inapplicability of spin stiffness and Gilbert damping measurement in thick (Ga,Mn)As epilayers

Finally, we illustrate the significance of the film magnetic homogeneity for a correct evaluation of the spin stiffness and Gilbert damping coefficient. For this purpose we selected a 500 nm thick (Ga,Mn)As epilayer with 7% Mn (i.e, a sample with the same nominal Mn doping as the one used in experiments depicted in Supplementary Figure S16). In Supplementary Figure S5(a) and (b) we show the temperature dependent magnetization projections to several crystallographic directions measured in the as-grown and annealed samples. In the as-grown sample, the temperature dependence of magnetization projections is strongly non-monotonous [see Supplementary Figure S5(a)]. Moreover, the Curie temperature T_c is only ≈ 60 K that is very low for a material with 7% Mn. This is a consequence of a high concentration of unintentional interstitial Mn impurities in the sample that compensate both the local moment and the holes produced by substitutional Mn atoms.[55] The amount of interstitial Mn impurities in the sample can be reduced by a thermal annealing.[54] However, even very long annealing times are not sufficient for obtaining a high quality sample from the thick epilayer due to the formation of the surface oxide that controls the outdiffusion of interstitial Mn impurities.[54] Therefore, the 40 h long annealing at 200 °C led to an increase of T_c but only to 90 K, which is still substantially lower than T_c ≈ 150 K observed in thin samples with the same nominal concentration of Mn. Simultaneously, the temperature

dependence of magnetization does not show the expected sharply vanishing magnetization at T_c (cf. Fig. 1(a) in the main paper where the SQUID data measured in the optimized epilayer are depicted). In Fig. 1(d) in the main paper we show the temperature dependence of the resistivity and its temperature derivative measured in the annealed sample. Clearly, there is no sharp Curie point singularity in the temperature derivative of the resistivity which is the fingerprint of a high magnetic quality of (Ga,Mn)As epilayer. In Supplementary Figure S5(c) and (d) we show the time-resolved magneto-optical signals measured in this 500 nm thick epilayer. In the as-grown sample two precession modes can be identified. In the annealed sample the improved magnetic quality leads to a strong suppression of the magnetization precession damping with respect to that observed in the as-grown sample. For example, the data shown in Supplementary Figure S5(c) and (d) for the lowest modes correspond to damping times of 210 ps and 460 ps for the as-grown and annealed sample, respectively (see also Fig. 1(b) and (e) in the main paper where the corresponding Gilbert damping coefficients are depicted). In addition, the annealing led to a considerable increase of the number of observed SWR modes in the measured TRMO signal. However, their identification is a rather complicated task. In Supplementary Figure S6(a) and (b) we show the FFT spectrum of the oscillatory MO signals measured in the annealed sample for external magnetic fields of 10 mT and 20 mT. Even though the magnetic field change was rather small, the FFT spectra were changed dramatically. In particular, at 10 mT there are 3 peaks with comparable intensities (and 5 peaks in total) while at 20 mT there is only 1 strong peak (and 4 peaks in total). In Supplementary Figure S6(c) we show the dependence of the frequency of SWR modes on the external magnetic field with a plausible assignment of the measured frequencies to four SWRs described in the previous chapter and to one non-propagating surface mode.[23] We note that the identification of the lowest mode for fields below 15 mT as the surface mode is based on the analysis reported in Ref. 23 – in particular, due to the observations that this mode is apparent only at certain external magnetic fields and that it has a smaller amplitude that the one assigned to the homogeneous precession [see Supplementary Figure S6(a)]. Following the analysis reported in the previous chapter, we can now proceed to the evaluation of the spin stiffness. In Supplementary Figure S6(d) the deduced values of ΔH_n are plotted as a function of n^2. The observed mode spacing deviates significantly from that expected for SWRs in a magnetically homogeneous film (see Supplementary Equation S18) which is another fingerprint of the magnetic inhomogeneity in this 500 nm thick epilayer.[21-24] Consequently, despite a large number of SWRs detected in this sample, they cannot be used for a direct determination of the spin stiffness.

Finally, we compare the frequency dependence of the damping parameter α of the lowest precession mode measured in the annealed 7% (Ga,Mn)As epilayers with a thickness of 18 nm and 500 nm (see Fig. 1(b) and (e) in the main paper). As discussed above, for the homogeneous thin epilayer we observed a rather typical (and weak)[12, 13, 129-131] dependence of α on f from which the intrinsic Gilbert damping – that corresponds to the frequency-independent part of α – can be precisely obtained. On the contrary, for the 500 nm thick epilayer the dependence α (f) is strongly non-monotonous and resemble the dependence observed in Heusler alloys that was explained as a consequence of the strong material inhomogeneity.[13]

Supplementary References

61. Ohno, H. Electric-field control of ferromagnetism. *Nature* **408**, 944-946 (2000).
62. Chiba, D. *et al.* Electrical manipulation of magnetization reversal in a ferromagnetic Semiconductor. *Science* **301**, 943-945 (2003).
63. Chiba, D. Magnetization vector manipulation by electric fields. *Nature* **455**, 515-518 (2008).
64. Owen, M. H. S. *et al.* Low-voltage control of ferromagnetism in a semiconductor p–n junction. *New J. Phys.* **11**, 023008 (2009).
65. Stolichnov, I. *et al.* Non-volatile ferroelectric control of ferromagnetism in (Ga,Mn)As. *Nature Mater.* **7**, 464-467 (2008).
66. Sawicki, M. *et al.* Experimental probing of the interplay between ferromagnetism and localization in (Ga, Mn)As. *Nature Physics* **6**, 22-25 (2010).
67. Munekata, H. *et al.* Light-induced ferromagnetism in III-V-based diluted magnetic semiconductor heterostructures. *J. Appl. Phys.* **81**, 4862-4864 (1997).
68. Koshihara, S. *et al.* Ferromagnetic order induced by photogenerated carriers in magnetic III-V semiconductor heterostructures of (In,Mn)As/GaSb. *Phys. Rev. Lett.* **78**, 4617-4620 (1997).
69. Ohno, Y. *et al.* Electrical spin injection in a ferromagnetic semiconductor heterostructure. *Nature* **402**, 790-792 (1999).
70. Tanaka, M. and Higo, Y. Large tunneling magnetoresistance in GaMnAs/AlAs/GaMnAs ferromagnetic semiconductor tunnel junctions. *Phys. Rev. Lett.* **87**, 026602 (2001).
71. Chiba, D. Matsukura, F. and Ohno, H. Tunneling magnetoresistance in (Ga,Mn)As-

based heterostructures with a GaAs barrier. *Physica* **E 21**, 966-969 (2004).

72. Saito, H., Yuasa, S., and Ando, K. Origin of the tunnel anisotropic magnetoresistance in $Ga_{1-x}Mn_xAs/ZnSe/Ga_{1-x}Mn_xAs$ magnetic tunnel junctions of II-VI/III-V Heterostructures. *Phys. Rev. Lett.* **95**, 086604 (2005).
73. Mattana, R. *et al.* Chemical profile and magnetoresistance of $Ga_{1-x}Mn_xAs/GaAs/AlAs/GaAs/Ga_{1-x}Mn_xAs$ tunnel junctions. *Phys. Rev.* **B 71**, 075206 (2005).
74. Chiba, D. *et al.* Current-driven magnetization reversal in a ferromagnetic semiconductor (Ga,Mn)As/GaAs/(Ga,Mn)As tunnel junction. *Phys. Rev. Lett.* **93**, 216602 (2004).
75. Yamanouchi, M. *et al.* Current-induced domain-wall switching in a ferromagnetic semiconductor structure. *Nature* **428**, 539-542 (2004).
76. Yamanouchi, M. *et al.* Velocity of domain-wall motion induced by electrical current in the ferromagnetic semiconductor (Ga,Mn)As. *Phys. Rev. Lett.* **96**, 096601 (2006).
77. J. Wunderlich, J. *et al.* Local control of magnetocrystalline anisotropy in (Ga,Mn)As microdevices: Demonstration in current-induced switching. *Phys. Rev.* **B 76**, 054424 (2007).
78. Adam, J. *et al.* Nonadiabatic spin-transfer torque in (Ga,Mn)As with perpendicular anisotropy. *Phys. Rev.* **B 80**, 193204 (2009).
79. Wang, K. Y. *et al.* Current-driven domain wall motion across a wide temperature range in a (Ga,Mn)(As,P) device. *Appl. Phys. Lett.* **97**, 262102 (2010).
80. Curiale, J. *et al.* Spin drift velocity, polarization, and current-driven domain-wall motion in (Ga,Mn)(As,P). *Phys. Rev. Lett.* **108**, 076604 (2012).
81. Garate, I. *et al.* Nonadiabatic spin-transfer torque in real materials. *Phys. Rev.* **B 79**, 104416 (2009).
82. Hals, K. M. D., Nguyen, A. K., and Brataas, A. Intrinsic coupling between current and domain wall motion in (Ga,Mn)As. *Phys. Rev. Lett.* **102**, 256601 (2009).
83. Wenisch, J. *et al.* Control of magnetic anisotropy in (Ga,Mn)As by lithography-induced strain relaxation. *Phys. Rev. Lett.* **99**, 077201 (2007).
84. Rushforth, A. W. *et al.* Voltage control of magnetocrystalline anisotropy in ferromagnetic-semiconductor-piezoelectric hybrid structures. *Phys. Rev.* **B 78**, 085314 (2008).
85. Overby, M. *et al.* GaMnAs-based hybrid multiferroic memory device. *Appl. Phys. Lett.* **92**, 192501 (2008).
86. Goennenwein, S. T. B. *et al.* Piezo-voltage control of magnetization orientation in a ferromagnetic semiconductor. *phys. stat. sol.* (**RRL**) **2**, 96-98 (2008).

87. Ciccarelli, C. *et al.* Spin gating electrical current. (2012), arXiv:1203.2439.
88. Sinova, J. and Zutic, I. New moves of the spintronics tango. *Nature Mater.* **11**, 368-371 (2012).
89. Gould, C. *et al.* Tunneling anisotropic magnetoresistance: A spin-valve-like tunnel magnetoresistance using a single magnetic layer. *Phys. Rev. Lett.* **93**, 117203 (2004).
90. Moser, J. *et al.* Tunneling anisotropic magnetoresistance and spin-orbit coupling in Fe/GaAs/Au tunnel junctions. *Phys. Rev. Lett.* **99**, 056601 (2007).
91. Park, B. G. *et al.* A spin-valve-like magnetoresistance of an antiferromagnet-based tunnel junction. *Nature Mat.* **10**, 347-351 (2011).
92. Wunderlich, J. *et al.* Coulomb blockade anisotropic magnetoresistance effect in a (Ga,Mn)As single-electron transistor. *Phys. Rev. Lett.* **97**, 077201 (2006).
93. Bernand-Mantel, A. *et al.* Anisotropic magneto-Coulomb effects and magnetic single-electron-transistor action in a single nanoparticle. *Nat. Phys.* **5**, 920-924 (2009).
94. Chernyshov, A. *et al.* Evidence for reversible control of magnetization in a ferromagnetic material by means of spin–orbit magnetic field. *Nature Phys.* **5**, 656-659 (2009).
95. Miron, I. M. *et al.* Current-driven spin torque induced by the Rashba effect in a ferromagnetic metal layer. *Nature Mat.* **9**, 230-234 (2010).
96. Fang, D. *et al.* Spin–orbit-driven ferromagnetic resonance. *Nature Nanotech.* **6**, 413-417 (2011).
97. Chapman, R. A. and Hutchinson, W. G. Photoexcitation and photoionization of neutral manganese acceptors in gallium arsenide. *Phys. Rev. Lett.* **18**, 443-445 (1967).
98. Blakemore, J. S. *et al.* Thermal activation energy of manganese acceptors in gallium arsenide as a function of impurity spacing. *J. Appl. Phys.* **44**, 3352-3354 (1973).
99. Bhattacharjee, A. K. and Benoit a la Guillaume, C. Model for the Mn acceptor in GaAs. *Solid State Commun.* **113**, 17-21 (2000).
100. Yakunin, A. M. *et al.* Spatial structure of an individual Mn acceptor in GaAs. *Phys. Rev. Lett.* **92**, 216806 (2004).
101. Madelung, O., Rössler, U. and Schulz, M. Impurities and defects in group IV elements, IV-IV and III-V compounds. Part b: Group IV-IV and III-V compounds, vol. 41A2b of *Landolt-Börnstein - Group III condensed matter* (Springer-Verlag, 2003).
102. Marder, M. P. Condensed matter physics (Wiley, New York, 2000), Supplementary material by author.

103. Harrison, W. A. Electronic structure and the properties of solids (Freeman, San Francisco, 1980).
104. Linnarsson, M. *et al.* Electronic structure of the GaAs:Mn_{Ga} center. *Phys. Rev.* **B 55**, 6938-6944 (1997).
105. Ohno, H. Properties of ferromagnetic III-V semiconductors. *J. Magn. Magn. Mater.* **200**, 110-129 (1999).
106. Campion, R. P. *et al.* The growth of GaMnAs films by molecular beam epitaxy using arsenic dimers. *J. Cryst. Growth* **251**, 311-316 (2003).
107. Jungwirth, T. *et al.* Character of states near the Fermi level in (Ga,Mn)As: Impurity to valence band crossover. *Phys. Rev.* **B 76**, 125206 (2007).
108. Matsukura, F., Ohno, H., and Dietl, T. in Handbook of Magnetic Materials, edited by K. H. J. Buschow (Elsevier, Amsterdam, 2002), vol. 14, p. 1.
109. Ruzmetov, D. *et al.* High-temperature Hall effect in $Ga_{1-x}Mn_xAs$. *Phys. Rev.* **B 69**, 155207 (2004).
110. Jungwirth, T. *et al.* Prospects for high temperature ferromagnetism in (Ga,Mn)As semiconductors. Phys. Rev. B 72, 165204 (2005).
111. Ferreira da Silva, A. *et al.* Electrical resistivity of acceptor carbon in GaAs. *J. Appl. Phys.* **95**, 2532 (2004).
112. Shklovskii, B. I. and Efros, A. L. Electronic properties of doped semiconductors (Spinger-Verlag, New York, 1984).
113. Lee, P. A. and Ramakrishnan, T. V., Disordered electronic systems. *Rev. Mod. Phys.* **57**, 287-337 (1985).
114. Paalanen, M. A. and Bhatt, R. N. Transport and thermodynamic properties across the metal-insulator transition. *Physica* **B 169**, 223-230 (1991).
115. Dietl, T. Origin of ferromagnetic response in diluted magnetic semiconductors and oxides. *J. Phys.: Condens. Matter* **19**, 165204 (2007).
116. Okabayashi, J. *et al.* Core-level photoemission study of $Ga_{1-x}Mn_xAs$. *Phys. Rev.* **B 58**, R4211- R4214 (1998).
117. Matsukura, F. *et al.* Transport properties and origin of ferromagnetism in (Ga,Mn)As. *Phys. Rev.* **B 57**, R2037 (1998).
118. J. Szczytko, J. *et al.* Antiferromagnetic p-d exchange in ferromagnetic $Ga_{1-x}Mn_xAs$ epilayers. *Phys. Rev.* **B 59**, 12935 (1999).
119. Omiya, T. *et al.* Magnetotransport properties of (Ga,Mn)As investigated at low temperature and high magnetic field. *Physica* **E 7**, 976-980 (2000).

120. Jungwirth, T. *et al.* Interlayer coupling in ferromagnetic semiconductor superlattices. Phys. Rev. B 59, 9818-9821 (1999).
121. Dietl, T. *et al.* Zener model description of ferromagnetism in zinc-blende magnetic semiconductors. *Science* **287**, 1019-1022 (2000).
122. Sato, K. *et al.* First-principles theory of dilute magnetic semiconductors. *Rev. Mod. Phys*. **82**, 1633-1690 (2010).
123. Brown, W. J. and Blakemore, J. S. Transport and photoelectrical properties of gallium arsenide containing deep acceptors. *J. Appl. Phys.* **43**, 2242-2246 (1972).
124. Woodbury, D. A. and Blakemore, J. S., Impurity conduction and the metal-nonmetal transition in manganese-doped gallium arsenide. *Phys. Rev.* **B 8**, 3803-3810 (1973).
125. Wang, K.-Y. *et al.* Spin reorientation transition in single-domain (Ga,Mn)As. *Phys. Rev. Lett*. **95**, 217204 (2005).
126. Liu, X. & Furdyna, J. K. Ferromagnetic resonance in $Ga_{1-x}Mn_xAs$ dilute magnetic semiconductors. *J. Phys. Cond. Matter.* **18**, 245-279 (2006).
127. Kobayashi, S., Hashimoto, Y. and Munekata, H. Investigation of an effective anisotropy field involved in photoinduced precession of magnetization in (Ga,Mn)As. *J. Appl. Phys.* **105**, 07C519 (2009).
128. Suda, K., Kobayashi, S., Aoyama, J., and Munekata H. Photo-onduced precession of magnetization in (Ga,Mn)As Microbars. *IEEE Trans. Magn.* **46**, 2421-2423 (2010).
129. Wu, J., Hughes, N.D., Moore, J.R., Hicken, R.J. Excitation and damping of spin excitations in ferromagnetic thin films. *J. Magn. Magn. Mater.* **241**, 96-109 (2002).
130. Djordjevic, M., Eilers, G., Parge, A., Münzenberg, M., Moodera, J. S. Intrinsic and nonlocal Gilbert damping parameter in all optical pump-probe experiments. *J. Appl. Phys.* **99**, 08F308 (2006).
131. Rzhevsky, A. A., Krichevtsov, B. B., Bürgler, D. E., and Schneider, C. M. Magnetization dynamics induced by ultrashort optical pulses in Fe/Cr thin films. *Phys. Rev.* **B 75**, 224434 (2007).
132. Woltersdorf, G., Buess, M., Heinrich, B., and Back, C. H. Time Resolved Magnetization dynamics of ultrathin Fe(001) films: Spin-pumping and two-magnon scattering. *Phys. Rev. Lett.* **95**, 037401 (2005).
133. Neudecker, I., Woltersdorf, G., Heinrich, B., Okuno, T., Gubbiotti G., and Back, C.H. Comparison of frequency, field, and time domain ferromagnetic resonance methods. *J. Magn. Magn. Mater.* **307**, 148-156 (2006).
134. Walowski, J., Müller, G., Djordjevic, M., Münzenberg, M., Kläui, M., Vaz C. A. F., and

Bland, J. A. C. Energy equilibration processes of electrons, magnons, and phonons at the femtosecond time scale. *Phys. Rev. Lett.* **101**, 237401 (2008).

135. Zou, X., Wu, J., Wong, P. K. J., Xu, Y. B., Zhang, R., Zhai, Y., Bunce, C., and Chantrell, R. W. Damping in magnetization dynamics of single-crystal Fe_3O_4/GaN thin films. *J. Appl. Phys.* **109**, 07D341 (2011).
136. Lenk, B., Eilers, G., Hamrle, J., and Münzberg, M. Spin-wave population in nickel after femtosecond laser pulse excitation. *Phys. Rev.* **B 82**, 134443 (2010).

137. Wang, D. M., Ren, Y. H., Liu, X., Furdyna, J. K., Grimsditch, M., and Merlin, R. Ultrafast optical study of magnons in the ferromagnetic semiconductor GaMnAs. *Superlatt. Microstruct.* **41**, 372-375 (2007).